

Metamorphoses of the flow past an obstacle of a resonantly driven bistable polariton fluid

Vincent Hakim, Simon Pigeon, Amandine Aftalion

▶ To cite this version:

Vincent Hakim, Simon Pigeon, Amandine Aftalion. Metamorphoses of the flow past an obstacle of a resonantly driven bistable polariton fluid. Physical Review B, 2023, 107 (4), pp.045306. 10.1103/PhysRevB.107.045306. hal-04306852

HAL Id: hal-04306852

https://hal.science/hal-04306852

Submitted on 12 Dec 2023

HAL is a multi-disciplinary open access archive for the deposit and dissemination of scientific research documents, whether they are published or not. The documents may come from teaching and research institutions in France or abroad, or from public or private research centers. L'archive ouverte pluridisciplinaire **HAL**, est destinée au dépôt et à la diffusion de documents scientifiques de niveau recherche, publiés ou non, émanant des établissements d'enseignement et de recherche français ou étrangers, des laboratoires publics ou privés.

Metamorphoses of the flow past an obstacle of a resonantly-driven bistable polariton fluid

Vincent Hakim*

Laboratoire de Physique de l'Ecole Normale Supérieure, CNRS, Ecole Normale Supérieure, PSL University, Sorbonne Université, Université Paris-Diderot, Paris, France

Simon Pigeon[†]

Laboratoire Kastler Brossel, Sorbonne Université, CNRS, Ecole Normale Supérieure, PSL University, Collège de France, Paris, France

Amandine Aftalion[‡]

Ecole des Hautes Etudes en Sciences Sociales, Centre d'Analyse et de Mathématique Sociales, UMR-8557, Paris, France. (Dated: January 11, 2023)

Motivated by recent experiments, we theoretically analyze the flow past an obstacle of a onedimensional "quantum fluid of light" which is resonantly driven, and exhibits bistability. The flow is found to abruptly change several times when the fluid velocity or the obstacle potential strength is increased. These transitions display unusual features. In contrast to the cases of usual fluids and superfluids, the transitions take place between stationary states. They involve the fluid bistability in an essential way. Remarkably, at the transitions points, the fluid in the obstacle wake lies in the unstable intermediate density state.

I. INTRODUCTION

The discovery of Bose-Einstein condensation has opened a very active field of research¹. Besides cold atomic vapors, Bose-Einstein condensation has also been achieved in exciton-polariton fluids^{2,3}. These "quantum fluids of light" ⁴ result from the strong coupling between the excitonic resonance of a semiconductor quantum well and a microcavity electromagnetic field. Their solid-state nature and the higher condensation temperature associated with the polariton very low mass turn them into attractive systems. In early experiments, polaritons were created with a transient⁵ or a spatially localized⁶ driving field to avoid interfering with the superfluid behavior of the condensate. The short polariton lifetime then restricted the experiment duration or limited the observations to a local region around the pumping spot. In order to bypass these limitations, it has been found useful to introduce a weaker resonant drive, a so-called "support field", away from the strong localized pumping spot used to create the polaritons⁷. The extended quasi-resonant drive tends to lock the phase of the condensate and its dynamics, which is different from the dynamics of a conventional fluid or of a superfluid⁸. When the support field is not too strong, it allows the formation of collective excitations, such as vortices⁹ and dark solitons¹⁰. This new coherently driven regime has started to be investigated theoretically^{3,7,11-13} and experimentally^{9,10,14,15}.

Here, we consider the flow of a resonantly-driven condensate past an obstacle. Such a set-up has been the subject of many investigations both for classical fluids¹⁶ and superfluids¹. In two or three dimensions, the flow becomes unsteady at a critical velocity through an oscillatory (Hopf) bifurcation. For superfluids, this leads

to the nucleation of vortices¹⁷ past the critical velocity. In a one-dimensional setting, gray solitons are generated and propagate from the obstacle along the flow¹⁸. For standard (conservative) superfluids, these dynamical behaviors are well-described in the framework of the Gross-Pitaevskii equation^{19–23}. If the creation of defects in the flow of a resonantly-driven condensate has been observed, strong deviation from standard superfluids behaviors were reported^{3,7,12,15}. It remains to better understand the transition and its dependence on the fluid bistability²⁴, and, more generally, condensate dynamics in the presence of resonant drive and dissipation.

In the present work, we focus on the one-dimensional case which is easier to analyze than higher dimensional cases. We find that multiple transitions in the flow occur when the fluid velocity is increased, or when the obstacle strength is increased at fixed velocity. We show that these transitions are of a very different type from the usual ones in fluids and superfluids. Moreover, their unusual character forbids their prediction from the characteristics of excitations around the steady flow, as done for superfluids with the Landau criterion ¹.

II. THE GENERALIZED GROSS-PITAEVSKII EQUATION AND BISTABILITY

We consider the fluid described by the following generalized Gross-Pitaevskii equation (GGPE)

$$i\hbar\partial_t\psi = \frac{-\hbar^2}{2m}\partial_x^2\psi + \left[V(x) - \hbar\Delta - i\frac{\hbar\gamma}{2} + g|\psi|^2\right]\psi + Fe^{ik_px}.$$
(1)

In the context of exciton-polariton microcavity physics, Eq. (1) provides an effective description of a driven lower polariton field^{3,4}, with the polariton-polariton repulsive interaction accounted by the constant q > 0. Additional terms as compared to the usual GPE arise from the coherent drive and dissipation^{3,4}. The support field is characterized by its amplitude F, its momentum k_p , produced by a slight tilt of the driving laser beam with respect to the cavity plane and the detuning Δ of its frequency from the lower polariton band bottom frequency. Dissipation is described by the rate $\gamma > 0$ arising from the polariton finite lifetime. The potential V(x) models a localized obstacle. It is our main aim to characterize its effect on the fluid flow described by Eq. (1). It is worth noting that our results are also relevant for nonlinear optics²⁵ where Eq. (1) is known as the Lugiato-Lefever equation²⁶ and describes the wave evolution in a cavity filled with a nonlinear medium (see e.g.²⁷ and ref. therein).

The explicit x-dependence in Eq. (1) can be eliminated by defining,

$$\psi = \sqrt{\hbar \gamma / 2g} \,\phi(x) \exp(ik_p x). \tag{2}$$

The function ϕ then obeys the equation,

$$i\partial_{\tau}\phi = -\frac{1}{2}\partial_{yy}\phi - ik_0\partial_y\phi - \left[\delta_V(y) + i - |\phi|^2\right]\phi + f, (3)$$

where we have introduced the dimensionless variables $y=x\sqrt{m\gamma/2\hbar},~\tau=t\gamma/2,~{\rm and~constants},~k_0=k_p\sqrt{2\hbar/m\gamma},f=F\sqrt{g}(2/\hbar\gamma)^{3/2}$, and defined the function

$$\delta_V(y) = \delta_0 - \frac{2}{\hbar \gamma} V(y)$$
, with $\delta_0 = \frac{2}{\hbar \gamma} \left[\hbar \Delta - \frac{(\hbar k_p)^2}{2m} \right]$.

Before considering the effect of a localized obstacle, we briefly recall some properties of the fluid described by Eq. (3). When V(y) = 0 and $\delta_V(y) = \delta_0$, Eq. (3) has constant solutions in space and time with a homogeneous density $\rho = |\phi|^2$ which can readily be seen to simply obey,

$$B(\rho) := [(\rho - \delta_0)^2 + 1]\rho = f^2.$$
 (5)

Two cases can be distinguished. When $\delta_0 < 0$, the function $B(\rho)$, defined in Eq. (5), is increasing from 0 to $+\infty$ with the density. As a consequence, the density ρ is also an increasing function of the forcing amplitude f. When $\delta_0 > 0$, namely for blue detuning, $B(\rho)$ can be non-monotonic with multiple homogeneous solutions for a given forcing. A simple analysis of Eq. (5) shows that this actually happens when $\delta_0 > \sqrt{3}$. An example of this S-like dependency of the density with the driving field is plotted in Fig. 1a. In this case, three solutions exist in a window of intermediate forcing strengths i.e. for $B(\rho_+) < f^2 < B(\rho_-)$ with

$$\rho_{\pm} = \frac{1}{3} \left(2\delta_0 \pm \sqrt{\delta_0^2 - 3} \right). \tag{6}$$

The high density (HD) and low density (LD) solutions are stable while the intermediate density (ID) one is unstable, as explicitly shown in Appendix A. Bistability stems

from the positive feedback between the fluid density increase and forcing efficiency, for blue detuning. When the density of the fluid increases, the detuning of the forcing decreases as a consequence of the repulsive self-interactions, as can explicitly be seen in Eq. (5). This results in a more closely resonant and thus more efficient forcing which, in turn, increases the fluid density. This bistability for sufficiently strong blue detuning is well-known in nonlinear optics⁴ and has been demonstrated for polaritons in microcavities²⁴. While in the LD state, self-interactions are unimportant, the strong self-interactions in the HD state modify the fluid flow properties^{8,28}.

III. FLOW PAST AN OBSTACLE : NUMERICAL SIMULATIONS AND FLOW METAMORPHOSIS

Having recalled the basic features of the homogeneous state, we proceed and describe our simulations of Eq. (3) with a localized repulsive (V(y) > 0) Gaussian potential

$$V(y) = \frac{\hbar \gamma}{2} u_m \exp[-(y/\sigma)^2]. \tag{7}$$

We focus on the bistable parameter regime with $\delta_0 > \sqrt{3}$ and the forcing f in the appropriate intermediate interval (see Fig. 1a). In an experimental setting, a strong driving field in a far upstream local region would be used to create the HD state as proposed in ref.⁷, experimentally realized in e.g. ¹⁵, and sketched in Fig. S1. Instead, here, we study an equivalent but mathematically simpler situation by simply setting up the fluid in the HD state as an upstream boundary condition.

Simulations of Eq. (3) with the Gaussian potential (7) are performed as in ref.²⁰ with a finite-difference semi-implicit Crank-Nicholson scheme. The reported results are obtained in a symmetric domain around the origin, of linear size 150 or 200, with a spatial step $\Delta y = 0.05$ and a time step $\Delta \tau = 10^{-4}$.

For a low potential amplitude, the flow is steady. The density decreases as expected in the region of the repulsive potential, and it returns smoothly to the HD state in the wake of the obstacle, as shown in Fig. 1b. For a weak potential, this configuration has been previously studied perturbatively in the context of a moving particle in a polariton fluid 29,30 . An increase in the potential amplitude u_m produces a transition in the flow, as shown in Fig. 1c. However, the character of the transition appears to be very different from the usual transitions to timedependent flows in fluids and superfluids. Instead, above the transition the flow is still stationary, after a transient, but with the fluid density in the LD state downstream of the obstacle, as shown Fig. 1c. In other words, for the driven-dissipative GGPE, the steady flow undergoes a metamorphosis instead of becoming time-dependent. That the flow density downstream of the obstacle lies in the LD state provides a first hint that the fluid bistability is playing a significant role in the observed transition.

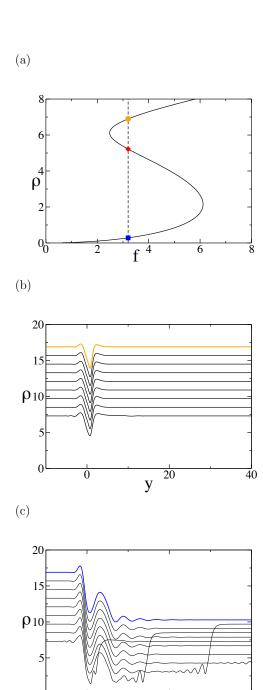


FIG. 1: Numerical simulations of Eq. (3). (a) Fluid density ρ vs. forcing f as described by Eq. (5). In the parameter regime considered, there are three homogeneous steady states, stable HD (high density, solid orange circle) and LD states (low density, solid blue square) and an unstable ID one (intermediate density, solid red diamond). The fluid is injected in the HD state. The fluid density is shown at successive times separated by $\Delta \tau = 6$. Succession sive curves are shifted upward with time by 1.2 unit of density to highlight that the flow becomes stationary. The last simulation curve is shown as a thicker colored line. (b) for a potential amplitude $u_m = 2$, the flow is steady with the wake of the obstacle in the HD state at $y \gg 0$. (c) For a larger $u_m = 6$, the flow is still stationary, but is in the LD state in the wake of the obstacle. Other parameters are $\delta_0 = 6.2, f = 3.2, k_0 = 2.75$ which corresponds to the typical experimental values $\hbar\Delta = 0.5 meV$, $\hbar\gamma = 0.1 meV$, $\hbar^2/m = 1 meV \mu m^2$, $k_p = 0.616 \mu m^{-1}$, $\sqrt{g}F = 0.036 (meV)^{3/2}$. The potential range is $\sigma = 1$ corresponding to $4.5\mu m$, the chosen unit length.

20

40

Simulations of Eq. (3) for different potential amplitudes u_m and different flow velocities k_0 , provide a more global view of the dynamical regimes of the GGPE flow past an obstacle, as summarized in Fig. 2. The results are displayed for two values of the potential range $\sigma = 1$ (Fig. 2a) and $\sigma = 2$ (Fig. 2b)³⁵ They are qualitatively very similar in the two cases. As expected, the transition point described above extends to a full boundary delimiting two domains in the (k_0, u_m) plane, with different kinds of steady state flow. In the outside domain (yellow domain in Fig. 2a,b), flows starting in the HDstate upstream of the obstacle return to the HD-state in the wake of the obstacle. On the contrary, in the inside domain (blue domain in Fig. 2a,b), flows starting in the HD-state end up in the LD-state in the wake of the obstacle. However, the survey of an extended part of the (k_0, u_m) plane brings a surprise : other transitions are found, corresponding in Fig. 2a,b to the boundaries of the smaller yellow regions inside the blue domain. In these smaller regions, the fluid in the wake of the obstacle is again in the HD-state. These multiple transitions are illustrated in Fig. 2c-h for $\sigma = 2$, by increasing the potential amplitude u_m at fixed flow velocity k_0 . The fluid density is in the HD-state in the wake of the obstacle for low u_m values. At a first critical value of u_m , the fluid in the obstacle wake jumps in the LD-state (Fig. 2c,d) as described above. When the potential amplitude is further increased a second transition is found, at which the fluid density in the obstacle wake, jumps back to the HD-state (Fig. 2)e,f). At a still higher value of u_m , there is a third transition, similar to the first one, where the fluid density in the obstacle wake returns to the LD-state (Fig. 2e,f).

How does the transition take place in the obstacle wake, between a steady flow in the HD-state and a solution in the LD-state, when parameters are varied? In order to shed light on this question, simulations very close to a transition point on the lowest transition line are shown in Fig. 3a-d , for the two potential ranges $\sigma=1$ and $\sigma=2$. The flow velocity k_0 is fixed and the amplitude u_m of the potential is varied.

As shown in Fig. 3a, for $\sigma = 2$, when the amplitude of the potential is close to, but below, the critical potential amplitude u_m^* , the obstacle is followed by a fluid region of length L, close to the intermediate density (ID) unstable state. This region terminates by a front that joins the ID-state to the more downstream HD-state. As the potential amplitude approaches u_m^* , this front stands farther downstream from the obstacle, with an increasing region of the fluid downstream of the obstacle in the unstable ID state. For potentials with an amplitude slightly greater than u_m^* , the complementary process is observed, as shown in Fig. 3b. As for subcritical potentials, the obstacle is followed by a fluid region in the unstable ID state but which terminates by a front joining it to the stable LD -state. When increasing the potential amplitude, this front stands closer to the obstacle. It reaches the obstacle and disappears, as soon as the potential amplitude

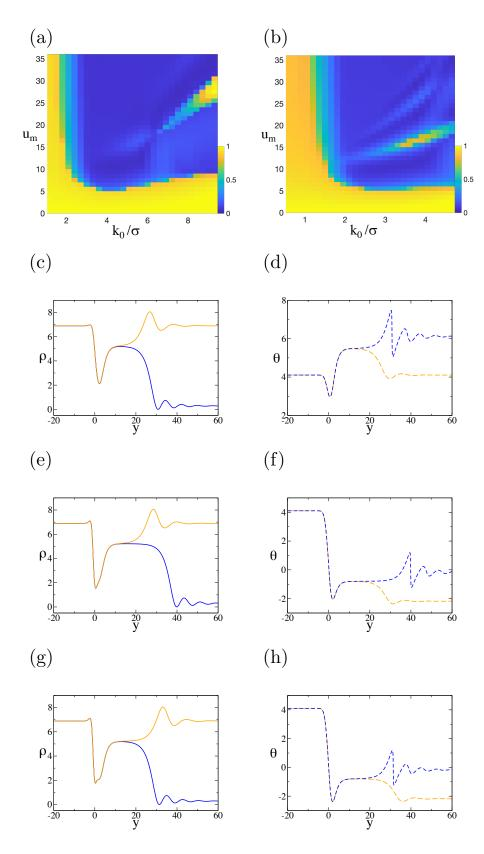


FIG. 2: Results of simulations of the GGPE (Eq. (1), (3)) for $f=3.2, \delta_0=6.2$ for different values of the localized potential amplitude u_m and velocity k_0 . The fluid is in the HD-state at $y\ll 0$. (a) The potential range is $\sigma=1$ in (a) and $\sigma=2$ in (b). The color code indicates the relative density in the wake of the obstacle relative to the density in the HD-state. Intermediate colors are due to the limited resolution of the numerical procedure used to scan this two-parameter plot. (c-h) For $\sigma=2$, close-up with higher resolution, of 3 transitions that take place when u_m is increased on the vertical line $k_0=6.4$ of panel (b). Solution densities ((c),(e),(g), solid lines) and phases ((d),(f),(h), dashed lines) are shown for two values of the potential just below and just above the transition. The fluid in the obstacle wake is either in the HD-state (orange) of the LD-state (blue). (c) & (d) 1st transition with $u_m=4.85$ (HD state) and $u_m=4.86$ (LD state) (e) &(f) 2nd transition with $u_m=14.16$ (LD state) and $u_m=14.17$ (HD state). The 2nd transition is inverted as compared to the 1st, namely the fluid density jumps back to the HD state when u_m is increased. (g) &(h) 3rd transition with $u_m=14.84$ (HD state) and $u_m=14.85$ (LD state). The

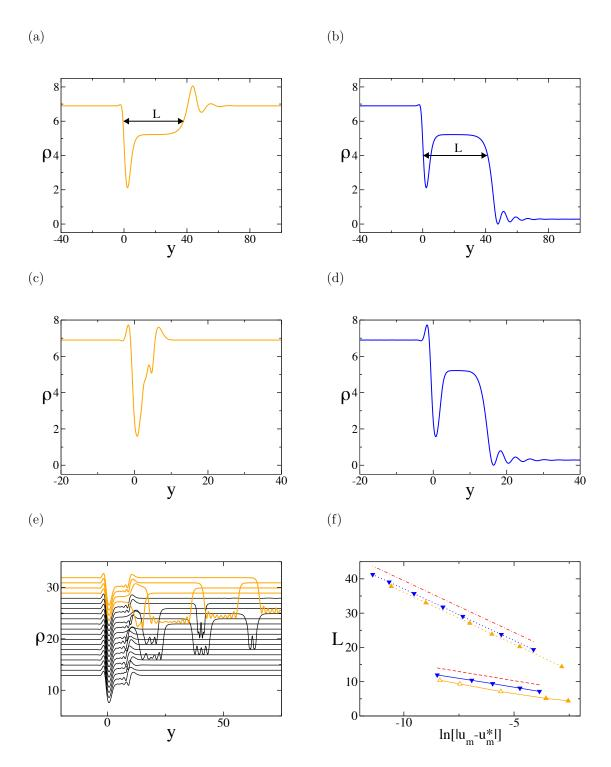


FIG. 3: Detail of the flow metamorphosis in simulations of Eq. (3). (a)&(b) $\sigma = 2, k_0 = 6.4$ with (a) $u_m = 4.8586914$, just below the transition with the fluid in the far wake of the obstacle in the HD-state, and (b) $u_m = 4.858728$, just above the transition with the fluid in the far wake of the obstacle in the LD-state (see [36])). In both cases, the fluid in the near wake of the obstacle is in the unstable ID-state, as described in the main text. (c), (d) & (e) Same as (a) and (b) for $\sigma = 1$ and three different potential amplitudes: (c) $u_m = 5.46$ below the transition, and (d) $u_m = 5.4789$, just above the transition. (e) For $u_m = 5.4781$, below but very close to the critical potential amplitude $u_m * \simeq 5.4786$, the fluid density is shown at successive times. The curves (dark solid lines) are plotted every 8 time units and shifted upward with time by 1 unit of density. The 4 last curves (thick orange solid lines) are highlighted in order to show the time dependence of the flow. (f) The length L of the ID state region (depicted in (a) & (b)) is shown as a function of $|u_m - u_m^*|$ for $u_m < u_m^*$ (upward-pointing triangle with orange dotted line) and $u_m > u_m^*$ (downward-pointing triangle with orange dotted line) when $\sigma = 2, k_0 = 6.4$ and $u_m * \simeq 4.8587$. The predicted asymptotic slope of -3.02 (Eq. (8) and Appendix A) is displayed (dashed-dotted red line). The length L is also shown when $\sigma = 1, k_0 = 2.75$ and $u_m^* \simeq 5.4786$ for $u_m < u_m^*$ for (upward-pointing triangles with solid orange line) or $u_m > u_m^*$ (blue solid line and downward-pointing triangle). when $\sigma = 1, k_0 = 2.75$ and $u_m^* \simeq 5.4786$. The predicted asymptotic slope of -1.07 is displayed (dashed red line). Filled symbols correspond to steady solutions. Empty symbols corresponds to time-dependent solutions and are only indicative since the fronts have significant oscillations. In both cases, the length L is defined as the distance from the potential maximum at y=0 to the point of density $\rho=6$ (resp. $\rho=4$) of the front joining the

departs by a small amount from u_m^* . These observations strongly suggest that the critical solution is such that the fluid downward wake exactly stands at the unstable ID-state.

For $\sigma = 1$, the scenario of the transition is similar but with an additional complication. When u_m approaches u_m^* from above, the ID to LD state stands farther and farther downstream from the obstacle with a large region of fluid in the ID state (Fig. 3d) exactly as for $\sigma = 2$. As in this previous case, this strongly suggests that the critical solution is such that the fluid density lies in the unstable ID state in the obstacle wake. When u_m is below u_m^* , and approaches it closely, the ID state appears in the obstacle wake together with a front linking it to the HD-state (Fig. 3c). However, the HD front recedes but becomes non-stationary, when u_m approaches even more closely u_m^* . This leads to large excursions in density, to and back from the LD-state, that travel in the far wake of the obstacle (Fig. 3e). This phenomenon which only takes place in a very small interval of u_m values below u_m^* is observed for different discretization steps, simulation box sizes and total simulation times. It thus appears real and not due to a numerical instability or to an incomplete relaxation to a steady state.

IV. CRITICAL SOLUTIONS EXISTENCE AND SHARPNESS OF THE TRANSITIONS

The transitions observed in the numerical simulations suggest that the critical flows are such that, surprisingly, the fluid lies in the unstable ID-state in the far wake of the obstacle. This leads us to consider at which conditions such steady solutions of Eq. (3) that start in the HD-state at $y=-\infty$ and end in the LD-state at $y=+\infty$ can exist. Another remarkable fact is the sharpness of the observed transitions when the potential strength u_m is varied (see e.g the very small difference between the values of u_m in Fig. 3a and b). We show below that considering the spatially growing modes around the homogeneous states at $y=-\infty$ and $y=+\infty$ sheds light on both questions.

A stationary solution of Eq. (3) obeys a 2nd-order complex equation. Thus, its asymptotic behavior around a homogeneous state is described by 4 real modes. As shown in Appendix A, three of these four modes are spatially diverging as $y \to +\infty$ when the stationary solution is linearized around the ID-state. Similarly, there are two diverging modes as $y \to -\infty$ when the solution is linearized around the HD-state. Let us suppose integrating in space the time independent version of Eq. (3) from the HD-state at $y = -\infty$. In order for the solution to tend towards the ID-state at $y = +\infty$, the prefactors of the three diverging modes should be set to zero. However, the only integration freedom lies in the prefactors of the two convergent modes at $y = -\infty$ since the amplitudes of the two divergent modes at $y = -\infty$ are set to zero by the initial condition. The solution can tend towards

the ID-state at $y=+\infty$ only if the potential amplitude is used as an additional variable to be adjusted to cancel the three divergent modes. Therefore, a stationary solution linking the HD-state at $y=-\infty$ to the ID-state at $y=+\infty$, only exists for a discrete set of critical potential amplitudes when other parameters are fixed. The numerics of Fig. 2 shows that this set actually comprises several values. We also show it analytically in section C, in a suitable asymptotic limit.

The whole process of the ID-state appearance in the wake of the obstacle, for u_m below u_m* , to its disappearance for u_m above u_m^* , takes place in a very small interval of values of the potential amplitude (Fig. 3a-d). This is a direct consequence of the ID-state instability, as we now show. When u_m is close to the critical amplitude u_m^* , the stationary solution $\phi(y)$ of Eq. (3) is close to the critical solution $\phi^*(y)$ for negative y and for positive y in the vicinity of the obstacle. Namely, on a length scale of order one behind the obstacle, one has $|\phi(y) - \phi^*(y)| \sim |u_m - u_m^*|$. This is also the magnitude of the 3 divergent modes in the vicinity of the potential. Behind the obstacle, the distance between $\phi(y)$ and $\phi^*(y)$ grows exponentially and is dominated by the rate q_{+} of the fastest growing mode, computed in Appendix A. The front in the obstacle wake, which links the IDstate to one of the homogeneous stable states (Fig. 3a-b), appears when $|\phi(y) - \phi^*(y)|$ reaches a value of order one. As a consequence, the distance L of the front from the obstacle is related to the difference $|u_m - u_m^*|$ between the potential amplitude and the critical one by,

$$|u_m - u_m^*| \exp(q_+ L) = O(1).$$
 (8)

This explains the sharpness of the transition observed in the numerical simulations (Fig. 3a-d) since in order to obtain a front at a distance L from the obstacle, u_m should be exponentially close in L to u_m^* . Conversely, the distance of the front from the obstacle only grows logarithmically with the departure of u_m from the critical potential amplitude, as

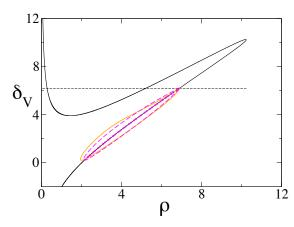
$$L \sim (-1/q_+) \ln |u_m - u_m^*|.$$
 (9)

The measured distance L is plotted vs. $\ln |u_m - u_m^*|$ in Fig. 3f, for u_m close to the critical potential and two values of k_0 . The asymptotic slope, $-1/q_+$, is also drawn, using the spatial growth rates computed in Appendix A. The quantitative agreement appears very good³⁶.

V. ANALYSIS OF THE TRANSITION: SLOWLY-VARYING OBSTACLES

In order to better understand these transitions and the role of bistability in the stationary flow metamorphosis, we consider the parameter regime suitable for theoretical analysis, provided by an obstacle that varies on a long length scale, $\sigma \gg 1$ (Eq. (7)). For a slowly varying obstacle, when the flow is accordingly slowly varying, the





(b)

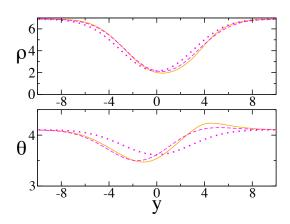


FIG. 4: Adiabatic approximation and corrections for the GGPE (Eq. (3)). (a) Plot in the (ρ, δ_V) diagram. (b) Plot of the density and the phase vs. y. The stationary numerical solution (orange solid line) of Eq. (3) is plotted together with the adiabatic solution alone (dotted magenta; Eq. (10),(11)) or with the first-order corrections (dashed magenta; Eq. (12)). The parameters are $\sigma=4,\ u_m=6,\ k_0=2.75,\ f=3.2, \delta_0=6.2.)$

derivative terms in Eq. (3) can be treated perturbatively. At the lowest order, they can be entirely neglected and the "adiabatic" solution, $\phi_a(y) = \sqrt{\rho_a(y)} \exp[i\theta_a(y)]$, readily obtained. The fluid density ρ_a , is linked to the potential amplitude by Eq. (5) with δ_0 simply replaced by $\delta_V(y)$ (Eq. (4)), which takes into account the influence of the potential on the detuning. In this adiabatic approximation, solving the quadratic Eq. (5) for $\delta_V(y)$ provides the implicit relation between the fluid density

and the potential,

$$\delta_V(y) = \rho_a(y) - \sqrt{\frac{f^2}{\rho_a(y)} - 1}, \quad 0 \le \rho_a \le f^2.$$
 (10)

As for homogeneous solutions, the solution phase is simply given as a function of the density

$$\theta_a(y) = \arctan\left(\frac{1}{\rho_a(y) - \delta_V(y)}\right)$$
 (11)

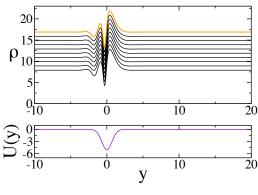
The relation (10) between the density ρ and the "detuning" δ_V at fixed forcing amplitude f, is plotted in Fig. 4a. It is equivalent but more convenient for our purpose than Fig. 1a, which gives the density as a function of f for fixed detuning. A simple calculation shows that Eq. (10) determines the density as a unique function of δ_V when $f < f_c = (4/3)^{3/4} \simeq 1.2408$ while for $f > f_c$, there is a range of δ_V values with multiple possible densities. In other words, bistability occurs for a range of δ_V values when $f > f_c$, as illustrated in Fig. 4a.

Let us now consider, a fluid injection in the HD-state, when the forcing is sufficiently strong for bistability to occur (i.e. $f > f_c$). As the potential varies with the position y, $\delta_V(y)$ follows it according to Eq. (4). The density, as given by Eq. (10), moves along the HD branch in Fig. 4a. The adabatic solution is already a close approximation of the flow obtained by numerically solving Eq. (3), for the Gaussian potential of Eq. (7) even with a rather large amplitude ($u_m = 6$) when $\sigma = 4$ (Fig. 4b).

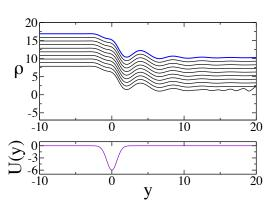
A. The attractive potential case

We first briefly describe the case of an attractive potential $(u_m < 0)$. Eq. (10) predicts that the fluid density goes up the high density branch in Fig. (4, as V(y) becomes more negative. The flow should undergo a transition if $|u_m|$ is large enough for the top of the high density branch to be reached, since the branch cannot be followed beyond its top. This transition is indeed seen in numerical simulations of Eq. (3) even away for the slowlyvarying potential limit, as shown for $\sigma = 1$ in Fig. 5. As for repulsive potentials, for small $|u_m|$, the flow is stationary and in the HD-state in the wake of the obstacle (Fig. 5a). There is a transition for a critical amplitude $u_{m,1}$. When $|u_m|$ is larger than the critical amplitude $|u_{m,1}|$, the flow in the wake of the obstacle is in the LDstate. The transition has however a different character than for repulsive potentials. The HD-state solution disappears at $u_{m,1}$ presumably by merging with an unstable solution in a classical saddle-node bifurcation. The LD-state solution exists and is stable below below $u_{m,1}$. It disappears at $u_{m,2}$. Both solutions co-exist (Fig. 5c) when u_m stands in between the two critical amplitudes, for $u_{m,1} < u_m < u_{m,2} < 0$, which is therefore an interval of flow bistability.

(a)



(b)



(c)

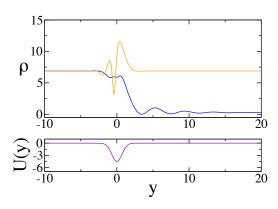


FIG. 5: Transition in the GGPE for an attractive potential. Simulations of (Eq. 3) for two localized potential amplitudes (a) $u_m = -5$ (b) $u_m = -6$. The density is shown at different times (solid black lines) with a time interval $\Delta \tau = 5$ between the different curves. The last simulation solution is plotted with a thicker line in (a) (orange solid line) and (b) (blue solid line). Successive curves have been shifted upward with time by 1 ρ -unit to show the stationarity of the flow. Note that the fluid beyond the obstacle is in the HD-state in (a) and in the LD-state in (b). (c) The HD-state (orange solid line) and LD-state (blue solid line) solutions coexist in for $-5.1 \le u_m \le -4.1$. They are displayed here for $u_m = -4.5$. For each simulation, the dimensionless attractive Gaussian potential U(y) is also shown (violet solid line), where U(y) = $2V(y)/(\hbar\gamma)$ (Eq. (6)). The other parameters are $f=3.2, \delta_0=$ $6.2, k_0 = 2.75, \sigma = 1.$

B. The repulsive potential case: a spatial rate-dependent tipping bifurcation

How a transition can happen for a repulsive potential $(u_m > 0)$ is less obvious. The density of the adiabatic solution (Eq. (10)) follows the high density branch towards low density before increasing again in the wake of the obstacle, as shown in Fig. 4a. This appears to be a smooth process for all potential strengths u_m . It is not clear why this would result in a transition of the flow profile at a critical amplitude u_m and what this critical amplitude would be. However, one can note that in the adiabatic approximation, all derivatives are absent and, as a consequence, the fluid velocity plays no role. This suggests to go beyond the adiabatic approximation and treat perturbatively the derivatives terms. Writing $\rho(y) = \rho_a(y) + \rho_1(y) + \cdots, \theta(y) = \theta_a(y) + \theta_1(y) + \cdots,$ the first corrections to the adiabatic solution of Eq. (10), (11) are obtained after a short calculation (see Appendix B) as,

$$\rho_1(y) = -\frac{2k_0}{B'(\rho_a)} \frac{d\rho_a}{dy}, \ \theta_1(y) = \frac{k_0}{B'(\rho_a)} \frac{d}{dy} [\delta_V(y) - 2\theta_a]$$
(12)

where $B'(\rho)$ denotes the derivative of $B(\rho)$ (Eq. (5)) with respect to ρ . These corrections are shown in Fig. 4b and, as expected, they result in a closer agreement between the analytic approximations and the numerical profiles. More interestingly, the corrected density profile in the (ρ, δ) diagram provides a clue to the origin of the instability (Fig. 4a). One observes that the correction (12) produces a departure of the profile from the high density branch towards the middle unstable branch when the potential returns to 0, in the close downward wake of the obstacle. Eq. (12) shows that this non-adiabatic effect grows with k_0 and, it also grows with the localized potential amplitude u_m . One can therefore guess, that, for sufficiently large u_m or k_0 , this leads the flow profile loop in Fig. 4a, to reach the unstable density branch in the (ρ, δ) diagram and leads to an instability. The global character of the bifurcation shows that it is invisible to linear (i.e. Bogoliubov) excitations 13,14,31 around the steady flow. It cannot be located by a criterion that only involves them, like the Landau criterion for superfluids. The bifurcation appears to be the analog in the spatial domain of "rate-dependent tipping" bifurcations ^{32,33} in bistable systems which have become of interest in the context of climate change.

C. Multiple transitions in a reduced asymptotic description.

While suggestive, the above argument is not rigorous since the perturbative correction (12) cannot be trusted when it is not small. In order to obtain a full reduced non-linear description, a further asymptotic limit is needed, beyond that of a slowly varying potential (i.e. $\sigma \to \infty$).

A simple mathematical one is obtained by increasing the flow velocity k_0 at the same time as the length scale of the potential is varied, i.e. taking the limit, $\sigma \to \infty$, $k_0 \to \infty$ with a fixed ratio $\kappa = k_0/\sigma$. Determining the steady solution of Eq. (3) reduces in this limit to solving the simple system,

$$\kappa \partial_z \rho = -2\rho - 2f\sqrt{\rho}\sin(\theta) \tag{13}$$

$$\kappa \partial_z \theta = [\delta_V(z) - \rho] - f \cos(\theta) / \sqrt{\rho}$$
 (14)

where $z = y/\sigma$. Eq. (13), (14) simply give back for $\kappa = 0$ the adiabatic solution (10),(11) and, perturbatively for small κ , the correction (12). But, in the asymptotic limit considered, κ can now take any value. The reduced system (13),(14), has only first-order derivatives in z. Eq. (13), (14), have only one spatially-divergent mode from the unstable ID-state at $z = +\infty$. A simple shooting method thus determines the critical amplitude of the potential, u_m^* , for which this divergence vanishes and the solution tends at $z = +\infty$ toward the ID branch, as illustrated in Fig. 6a. For given driving parameters, multiple transitions are found by increasing the localized potential amplitude, as for the full GGPE. The fluid density in the wake of the obstacle is in the HD-state for low potential amplitudes. At a first critical amplitude, it jumps to the LD-state, as described above. When the potential amplitude is further increased, a second transition is found, at which the fluid density jumps back to the HD-state. Further transitions are found for still higher values of u_m . The loci of these transitions are plotted in the (k_0, u_m) parameter plane in Fig. 6b.

For the reduced Eq. (13), (14), these multiple solutions and the asymptotics of the $u_m^*(k_0)$ branches can be analytically described by considering the large κ -limit. It is helpful to return to the complex function $\phi = \sqrt{\rho} \exp(i\theta)$ and analyze the dynamics of ρ and θ in the complex ϕ plane. For large κ , the evolution of ρ and θ with z is slow, except for the potential term $\delta_V(z)$ that evolves with z on a scale of order 1. Apart from this fast action of the potential, the dynamics is governed by the phase plane of the problem without potential $(\delta_V(y) = \delta_0)$. It is plotted in Fig. 7a together with the 3 fixed points and a few trajectories. In the presence of the potential, a solution, that starts in the HD-state at $z=-\infty$, remains in the HD-state until it encounters the localized potential. The potential does not explicitly appear in Eq. (13) that governs the evolution of the density. The density change produced by the potential is mediated by the change of the phase θ . It is smaller than it by a factor κ , on the length scale of order 1 where the potential has a significant amplitude. Therefore, at lowest order, the density does not change, on this length scale of order 1. On the contrary, Eq. (14) shows that the phase θ rotates by an angle $\Delta\theta$,

$$\Delta\theta = -\frac{2}{\hbar\gamma\kappa} \int_{-\infty}^{+\infty} dz \, V(z) = -\sqrt{\pi} \, u_m/\kappa \tag{15}$$

where the second equality holds for the Gaussian potential (7). Since the density is conserved, the action of the

potential is simply to displace ϕ on the circle of radius $r_H = \sqrt{\rho_H}$, where ρ_H is the density of the HD-state, as shown in Fig. 7b. For the solution to end up at $z = +\infty$ in the ID-state, the phase turn $\Delta\theta$ has to bring ϕ precisely, on one of the two entering separatrices of the unstable ID-state, namely at their crossing points points S_A or S_B , with the circle of radius r_H , as shown in Fig. 7b. Therefore, $\Delta\theta$ should be equal to $\theta_{A,B} - 2n\pi$, $n = 0, 1, \cdots$ where $\theta_{A,B}$ are the rotation angles corresponding to the displacement of the HD-state onto S_A or S_B (Fig. 7b) . The angle values with $n \geq 1$ correspond to the solution phase making full rotations before reaching one of the two separatrices. The double series of critical potential amplitudes for $\kappa \gg 1$, follows from Eq. (15),

$$u_m^* = -\kappa (\theta_{A,B} - 2n\pi)/\sqrt{\pi} + O(1) \quad n = 0, 1, 2, \cdots$$
 (16)

For the parameter values of Fig. 6 & 7 one has θ_A \simeq $-1.851, \theta_B \simeq -4.589$. Eq. (16) shows that asymptotically the critical potential amplitudes u_m^* depend linearly on $\kappa = k_0/\sigma$. Eq. (16) gives the slopes of the asymptotic lines of critical potential amplitudes as a function of κ . In order to fully obtain the asymptotic lines, one also needs to compute the constant, next-order, term in the large κ - expansion of u_m^* , as derived in Appendix C. The obtained asymptotic lines for the three lowest branches, with the slopes given by Eq. (16) and the intercepts at the origin given by Eq. (C14), are displayed in Fig. 6b together with the numerically obtained solutions. The two lowest transition branches merge at $\kappa \simeq 1.30$. The 4th and higher branches cross and recombine at intermediate κ values, producing the bifurcation diagram shown in Fig. 6b.

Finally, one can note that Fig. 6b resembles Fig. 2a,b for the full GGPE where σ is not large. One difference is that the band H1 in Fig. 6b terminates and does not exist at low κ values in Fig. 2a,b, presumably due to the recombination of the 2nd (H0 \rightarrow L1) and 3rd transition (H1 \rightarrow L1). For higher values of κ , the transition lines in the full GGPE are close to that of the reduced model.

VI. CONCLUSION

In summary, the presence of an extended resonant drive and the bistability that it creates, deeply change the transition of a condensate flowing past an obstacle. The stationary flow profile undergoes a metamorphosis through the spatial analog of a rate-dependent tipping bifurcation instead of becoming time-dependent. The metamorphosis takes place in a very small range of obstacle strengths (or velocities) due to the unstable nature of the wake at the transition. Moreover, for given flow and pumping parameters, successive transitions exist at a discrete number of potential amplitudes. We have shown that this can be understood analytically in a suitable asymptotic regime.

It is worth emphasizing that the bifurcations of the flow profile that we have described, are quite different from usual textbook bifurcations. The steady state solution does not disappear by merging with an unstable solution, like in a saddle-node bifurcation, the bifurcation which, for instance, gives rise to grey soliton emission in a one-dimensional condensate flow past and obstacle. The steady state above the bifurcation is also obviously different from the limit cycle in a Hopf bifurcation which gives rise to vortex emission in usual fluid flow or higher dimensional condensates. Here, the steady solution persists through the bifurcation. It is stable above the bifurcation but its shape has abruptly changed. The stationary solution undergoes a metamorphosis at the bifurcation point, in a way that is only possible in an infinite dimensional system, namely by deforming at infinity.

The results suggest a careful reexamination of the analogous flow transition in higher dimensions. We hope that they will also motivate experimental studies of the phenomenon. It will certainly be challenging to experimentally resolve the details of the transitions and to witness the appearance of the unstable state in the wake of the obstacle since this happens in a small neighborhood of the transition points. However, the transitions from a fluid in the HD-state to a fluid in the LD-state in the wake of the obstacle and the steadiness of the flow both below and above the transitions should be more easily observable. Finally, we cannot help but wonder, whether the extended switches of the fluid density wake induced by a localized obstacle could provide useful applications in all-optical technology and devices³⁴.

Acknowledgments

We would like to thank A. Bramati, E. Giacobino, K. Guerrero and M. Jacquet for fruitful discussions. VH is also thankful to H Chaté, T Geisel and the Heraeus foundation for their invitation to a workshop in Les Houches and the opportunity to learn about rate-dependent tipping bifurcations in other contexts.

Appendix A: Stability of the constant density solutions

Here and in the following appendices, we find it convenient to analyze the GGPE (Eq. (3)) by writing its solution ϕ as $\phi(y) = r(y) \exp[i\theta(y)]$, where the modulus r(y) is the square root of the fluid density $\rho(y)$, $r(y) = \sqrt{\rho(y)}$. With these notations, the adimensionned GGPE (Eq. (3)) gives for the modulus r and phase θ ,

$$\partial_{\tau}r = -\frac{1}{2}[2\partial_{y}\theta \,\partial_{y}r + r\partial_{yy}\theta] - k_{0}\partial_{y}r - r - f\sin(\theta)$$

$$r\partial_{\tau}\theta = \frac{1}{2}[\partial_{yy}r - r(\partial_{y}\theta)^{2}] - k_{0}r\partial_{y}\theta$$

$$+(\delta_{V}(y) - r^{2})r - f\cos(\theta)$$
(A1)

We first analyze the stability of the constant homogeneous solutions without potential ($\delta_V = \delta_0$). Their

modulus r_0 and phase θ_0 obviously obey

$$r_0 = -f\sin(\theta_0), (\delta_0 - r_0^2)r_0 = f\cos(\theta_0).$$
 (A2)

Taking the square of each of these two equations and adding them, gives back the previous Eq. (5).

Linearization of the dynamical system (A1) around one such constant solution, $r = r_0 + r_1$, $\theta = \theta_0 + \theta_1$, shows that the first-order terms r_1 and θ_1 obey,

$$(\partial_{\tau} + k_0 \partial_y) r_1 = -\frac{r_0}{2} \partial_{yy} \theta_1 - r_1 - f \cos(\theta_0) \theta_1$$
 (A3)
$$r_0 (\partial_{\tau} + k_0 \partial_y) \theta_1 = \frac{1}{2} \partial_{yy} r_1 + (\delta_0 - 3r_0^2) r_1 + f \sin(\theta_0) \theta_1$$

Since the linear system (A3) is invariant by translation, we can look for the eigenvectors as Fourier modes, under the form $r_1(y,t) = \overline{r}_1 \exp(st+iky), \theta_1 = \overline{\theta}_1 \exp(st+iky)$. The evolution of $(r_1, r_0\theta_1)$ is governed by the matrix **S** which has $s + ikk_0$ as its eigenvalues, with

$$\mathbf{S} = \begin{pmatrix} -1 & -f\cos(\theta_0)/r_0 + k^2/2 \\ \delta_0 - 3r_0^2 - k^2/2 & +f\sin(\theta_0)/r_0 \end{pmatrix}$$
$$= \begin{pmatrix} -1 & r_0^2 - \delta_0 + k^2/2 \\ \delta_0 - 3r_0^2 - k^2/2 & -1 \end{pmatrix}$$
(A4)

The phase θ_0 has been eliminated in the second equality with the help of the fixed point equations (A2). The trace of **S** is negative, equal to -2. Therefore, the system is stable if and only if the determinant of **S** is positive,

$$\det(\mathbf{S}) = 1 - (r_0^2 - \delta_0 + k^2/2)(\delta_0 - 3r_0^2 - k^2/2)$$

= $B'(r_0^2) + k^2(2r_0^2 - \delta_0) + k^4/4$ (A5)

where the function $B(\rho)$ in the last equality is defined by Eq.(5). The stability at long wavelengths $(k \ll 1)$ simply depends on the sign of $B'(r_0^2)$ with $B'(r_0^2) < 0$ leading to instability. That is, when there are multiple solutions, the branch of intermediate values of r_0^2 is unstable, the other ones are stable to homogeneous perturbations.

For Eq. (9) and the counting argument of section III, the values of the spatial growth rates q = ik of stationary perturbations (e.g. with s = 0) are needed. They obey

$$B'(r_0^2) + 2qk_0 + (qk_0)^2 \left[1 - \frac{1}{k_0^2} (2r_0^2 - \delta_0)\right] + \frac{(qk_0)^4}{4k_0^4} = 0$$
 (A6)

In order to determine the spatial growth rates about the LD, ID and HD states, one should first compute the coefficients of Eq. (A6), namely the densities of the LD, ID and HD states and the corresponding values of the B function derivative. The three densities are the roots of Eq. (5). With our parameter choice of $f=3.2, \delta_0=6.2$, they are respectively equal to, $\rho_L=r_{0,L}^2\simeq 0.2845, \ \rho_I=r_{0,I}^2\simeq 5.219, \ \rho_H=r_{0,H}^2\simeq 6.896$. The corresponding $B'(\rho)$ are $B'(\rho_L)\simeq 32.63, B'(\rho_I)\simeq -8.276, B'(\rho_H)\simeq 11.089$.

For the ID-state, when $k_0 = 2.75$, the four roots qk_0 of Eq. (A6) are found to be equal to $\{-5.82, 1.62 -$

i11.1, 1.62 + i11.1, 2.58. Thus, as stated in the main text, there are 3 modes that exponentially grow with y. One is real positive and the two others are complex conjugate modes with a positive real part. The fastest spatially growing is the real mode $q_{+} = 2.58/k_{0} = 0.938$. The corresponding slope $1/q_{+} = 1.07$ is used to plot the asymptotics of the intermediate state length as function of the departure from the critical potential amplitude (Eq. (8)) in Fig. 3e (red dashed line). The situation is similar for $k_0 = 6.4$ with $k_0 q_+ = 2.12$ for the fastest growing mode. The corresponding slope $1/q_+ = 0.33$ is also shown in Fig. 3e (red dashed-dotted line). We note that for large k_0 , the case of interest for slowly varying potentials, Eq. (A6) for $s = qk_0$ reduces to the 2nd order equation for the growth rate s of an homogeneous perturbation of the ID-state. Namely, the fastest spatially growing perturbation simply corresponds to the advection of the unstable ID-state temporally growing mode.

For the HD-state, when $k_0 = 2.75$, the four roots qk_0 are found to be equal to $\{-5.26 - i \, 2.34, -5.25914 + i \, 2.34, \, 5.26 - i \, 7.0, \, 5.26 + i \, 7.0\}$. Therefore, there are two diverging modes when y tends towards $-\infty$ or $+\infty$, as stated in the main text.

Appendix B: Expansion for a slowly-varying potential.

We provide here a derivation of the expressions for the adiabatic solution modulus (Eq. (10)) and phase (Eq. (11)) and their first corrections (Eq. (12)). We suppose that the potential is slowly varying on an adimensioned length scale $\sigma \gg 1$ (as given by Eq. (7) for a Gaussian potential). We consider a stationary solution of the GGPE as written in Eq. (A1). We expands its modulus and phase as $r(y) = r_a(y) + r_1(y) + \cdots$, $\theta(y) = \theta_a(y) + \theta_1(y) + \cdots$ with r_1 and ϕ_1 of order $1/\sigma$. This gives

$$r_a(y) + f \sin[\theta_a(y)] = 0,$$
 (B1)
 $(r_a(y)^2 - \delta_V(y)) r_a(y) + f \cos[\theta_a(y)] = 0.$ (B2)

These are the same equations as those determining the constant solution with δ_0 replaced by $\delta_V(y)$. The modulus $r_a(y)$ of the slowly varying solution corresponding to the stable HD branch is given by Eq. (10).

The first-corrections $r_1(y)$ and $\phi_1(y)$ obey,

$$r_1(y) + f \cos[\theta_a(y)] \,\theta_1(y) = -k_0 \partial_y r_a,$$

$$(3r_a(y)^2 - \delta_V(y)) \,r_1(y) - f \sin[\theta_a(y)] \,\theta_1(y) = -k_0 r_a \partial_y \theta_a.$$

This 2×2 linear system is straightforwardly solved. The determinant of the matrix \mathcal{L} on the l.h.s. is

$$\det(\mathcal{L}) = -f \sin[\theta_a] - f \cos[\theta_a(y)] \left[3r_a(y)^2 - \delta_V(y) \right]$$

$$= r_a(y) \left(1 + \left[r_a(y)^2 - \delta_V(y) \right] \left[3r_a(y)^2 - \delta_V(y) \right] \right)$$

$$= r_A(y) B'[r_a(y)^2],$$
(B3)

where we have used Eq. (B1) and (B2) to express the phase in term of the modulus of the zeroth-order adiabatic solution and $B'(\rho) = dB/d\rho$ denotes the derivative of the function $B(\rho)$ (Eq. (5)). Similarly, the Cramer's determinant for r_1 is

$$\det(\mathcal{L}_r) = k_0 f \left(\partial_y r_a \sin[\theta_a(y)] + r_a \partial_y \theta_a \cos[\theta_a(y)] \right)$$
$$= k_0 f \partial_y \left(r_a \sin[\theta_a(y)] \right) = -k_0 \partial_y \left(r_a^2 \right), \quad (B4)$$

where we have again used Eq. (B1) in the last equality. The ratio the two determinants (B4) and (B3) provide the expression for the first correction to the modulus of the stationary slowly-vaying solution. Since the fluid density is the square of the modulus r, the first correction ρ_1 to the density is $\rho_1 = 2r_a r_1$. This finally gives Eq. (12).

Similarly, one can compute the first-order phase correction. The Cramer's determinant for θ_1 is.

$$\det(\mathcal{L}_{\theta}) = k_0[3r_a^2 - \delta_V(y)]\partial_y r_a - k_0 r_a \partial_y \theta_a$$

$$= k_0 f \sin(\theta_a)\partial_y \theta_a + k_0 r_a \partial_y \delta_V - k_0 r_a \partial_y \theta_a$$

$$= k_0 r_a \partial_a \delta_V - 2k_0 r_a \partial_y \theta_a.$$
 (B5)

The ratio of the expressions (B5) and (B3) for the two determinants gives Eq. (12) for θ_1 .

Appendix C: Asymptotics in the slowly-varying potential and large flow velocity limit.

We study the asymptotics for large κ of the reduced system described by Eq. (13), (14) with the potential U(y)

$$U(z) = u_m u(z) \tag{C1}$$

For our choice of a Gaussian potential (Eq. (7)), u(z) is simply $\exp(-z^2)$. We derive the leading estimation (Eq. (16)) of the critical potential amplitude as well as the subleading constant term $u_m^{*,1}$ in its $1/\kappa$ expansion,

$$u_m^* = \kappa u_m^{*,0} + u_m^{*,1} + \cdots$$
 (C2)

We seek the expansions of the solution modulus r(y) and phase $\theta(y)$, as well as the potential amplitude, under the form

$$r(z) = r_H + \frac{1}{\kappa} r_1(z) + \cdots, \qquad (C3)$$

$$\theta(z) = \theta_0(z) + \frac{1}{\kappa} \theta_1(y) + \cdots,$$
 (C4)

$$u_m = \kappa u_m^0 + u_m^1 + \cdots, \tag{C5}$$

with the boundary condition $\theta(-\infty) = \theta_H$, where r_H and θ_H are the phase and modulus of the HD-state.

At lowest order, Eq. (14) gives

$$\partial_y \theta_0 = -u_m^0 u(z)$$
, i.e. $\theta_0(z) = \theta_H - \int_{-\infty}^z dz' \, u_m^0 \, u(z')$, (C6)

while r remains constant equal to r_H . The critical potential amplitude u_m^* is such that the solution asymptotically land on the ID fixed point. At the considered lowest order in $1/\kappa$, this requires that the point (r_H, θ_0) should tend toward S_A or S_B (Fig. 7), the crossing points of the circle of radius r_H with the two entering separatrices of the ID fixed point. Namely $\theta_0(z)$ should tend toward θ_S , the angular coordinate of S_A or S_B when $z \to +\infty$. This gives for the critical potential amplitude,

$$\int_{-\infty}^{+\infty} dz \, u_m^{*,0} \, u(z) = \theta_H - \theta_S \text{ or } u_m^{*,0} = \frac{\theta_H - \theta_S}{\int_{-\infty}^{+\infty} dz \, u(z)}$$
 (C7)

where θ_S should be equal to $\theta_H + \theta_A - 2n\pi$ or $\theta_H + \theta_B - 2n\pi$ in agreement with Eq. (15). Numerically, for the parameters of Fig. 6 and Fig. 7, one has $\theta_A = -1.851$, $\theta_B = -4.462$ for the two separatrix points S_A and S_B . This gives for the asymptotic slopes of the first three bifurcation branches (Fig. 6),

$$u_{m,1st}^{*,0}=1.044,\ u_{m,2nd}^{*,0}=2.517,\ u_{m,3rd}^{*,0}=4.589.\ \ (\text{C8})$$

where $u_{m,3rd}^{*,0}$ corresponds to the angle $\theta_A - 2\pi$.

At the next order, the modulus r_1 and phase θ_1 are given by,

$$r_1(z) = -\int_{-\infty}^{z} dz' \{ r_H + f \sin[\theta_0^*(z')] \}$$

$$\theta_1(z) = \int_{-\infty}^{z} dz' \{ \delta_0 - r_H^2 - f \cos[\theta_0^*(z')] / r_H - u_m^1 u(z') \}$$
(C9)

where the *-superscript on $\theta_0(y)$ is meant to denote that $\theta_0^*(y)$ is the solution of Eq. (C6) for u_m^0 equal to $u_m^{*,0}$. The perturbation expansion used to obtain these expressions

is valid as long as $r_1(z)/\kappa$ and $\theta_1(z)/\kappa$ are small. Namely, z can be large but should be much smaller than κ . For $1 \ll z \ll \kappa$, Eq. (C9) and (C10) show that $r_1(z)$ and $\theta_1(z)$ grow linearly with z in a direction parallel to the separatrix at its crossing point with the circle of radius r_H ,

$$r_1(z) \sim s_r z, \ \theta_1(z) \sim s_\theta z$$
 (C10)

with

$$s_r = -r_H - f\sin(\theta_S), \ s_\theta = \delta_0 - r_H^2 - f\cos(\theta_S)/r_H \ (C11)$$

In order to reach the intermediate density point, the point $r(y), \theta(y)$ should belong to the separatrix when $y \gg 1$. This gives the condition,

$$\lim_{y \to +\infty} [s_{\theta} r_1(y) - s_r \theta_1(y)] = 0 \tag{C12}$$

It determines $u_m^{*,1}$, the subleading term in the expansion of the critical potential amplitude, as

$$u_{m}^{*,1} = \frac{1}{\int_{-\infty}^{+\infty} dz \, u(z)} \int_{-\infty}^{+\infty} dz \, \left(\delta_{0} - r_{H}^{2} - \frac{f}{r_{H}} \cos[\theta_{0}(y)] + \frac{s_{\theta}}{s_{r}} \left\{ r_{H} + f \sin[\theta_{0}(y)] \right\} \right) (C13)$$

For f=3.2, $\delta_0=6.2$, the modulus and phase of the HD-state are $r_H=2.626, \theta_H=-2.179$. With these values and the values of θ_A and θ_B , one obtains for the subleading constants in the first three bifurcation branch asymptotics

$$u_{m,1st}^{*,1} = 0.428, \ u_{m,2nd}^{*,1} = 5.074, \ u_{m,3rd}^{*,1} = -0.277.$$
(C14)

^{*} Electronic address: vincent.hakim@ens.fr

[†] Electronic address: simon.pigeon@lkb.upmc.fr

[‡] Electronic address: amandine.aftalion@ehess.fr

¹ L. Pitaevskii and S. Stringari, Bose-Einstein condensation and superfluidity, vol. 164 (Oxford University Press, 2016).

² J. Kasprzak, M. Richard, S. Kundermann, A. Baas, P. Jeambrun, J. M. J. Keeling, F. Marchetti, M. Szymańska, R. André, J. Staehli, et al., Nature 443, 409 (2006).

³ I. Amelio and I. Carusotto, Physical Review B **101**, 064505 (2020).

⁴ I. Carusotto and C. Ciuti, Reviews of Modern Physics **85**, 299 (2013).

G. Nardin, G. Grosso, Y. Léger, B. Pietka, F. Morier-Genoud, and B. Deveaud-Plédran, Nature Physics 7, 635 (2011)

⁶ A. Amo, S. Pigeon, D. Sanvitto, V. Sala, R. Hivet, I. Carusotto, F. Pisanello, G. Leménager, R. Houdré, E. Giacobino, et al., Science 332, 1167 (2011).

⁷ S. Pigeon and A. Bramati, New Journal of Physics 19, 095004 (2017).

⁸ R. Juggins, J. Keeling, and M. Szymańska, Nature com-

munications 9, 4062 (2018).

⁹ S. Koniakhin, O. Bleu, D. Stupin, S. Pigeon, A. Maitre, F. Claude, G. Lerario, Q. Glorieux, A. Bramati, D. Solnyshkov, et al., Physical Review Letters **123**, 215301 (2019).

A. Maitre, G. Lerario, A. Medeiros, F. Claude, Q. Glorieux, E. Giacobino, S. Pigeon, and A. Bramati, Physical Review X 10, 041028 (2020).

¹¹ I. Chestnov, A. Kavokin, and A. Yulin, New Journal of Physics 21, 113009 (2019).

¹² S. Pigeon and A. Aftalion, Physica D: Nonlinear Phenomena 415, 132747 (2021).

¹³ M. Joly, L. Giacomelli, F. Claude, E. Giacobino, Q. Glorieux, I. Carusotto, A. Bramati, and M. J. Jacquet, arXiv preprint arXiv:2110.14452 (2021).

¹⁴ P. Stepanov, I. Amelio, J.-G. Rousset, J. Bloch, A. Lemaître, A. Amo, A. Minguzzi, I. Carusotto, and M. Richard, Nature communications 10, 1 (2019).

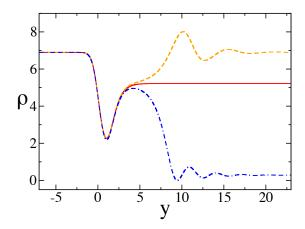
¹⁵ G. Lerario, A. Maître, R. Boddeda, Q. Glorieux, E. Giacobino, S. Pigeon, and A. Bramati, Physical Review Research 2, 023049 (2020).

¹⁶ C. Williamson, Annual Review of Fluid Mechanics 28, 477

- (1996).
- ¹⁷ C. Raman, M. Köhl, R. Onofrio, D. Durfee, C. Kuklewicz, Z. Hadzibabic, and W. Ketterle, Physical Review Letters 83, 2502 (1999).
- ¹⁸ P. Engels and C. Atherton, Physical Review Letters 99, 160405 (2007).
- ¹⁹ T. Frisch, Y. Pomeau, and S. Rica, Physical Review Letters 69, 1644 (1992).
- ²⁰ V. Hakim, Physical Review E **55**, 2835 (1997).
- ²¹ B. Jackson, J. McCann, and C. Adams, Physical Review A **61**, 013604 (1999).
- ²² C. Huepe and M.-E. Brachet, Physica D: Nonlinear Phenomena 140, 126 (2000).
- ²³ A. Aftalion, Q. Du, and Y. Pomeau, Physical Review Letters **91**, 090407 (2003).
- ²⁴ A. Baas, J. P. Karr, H. Eleuch, and E. Giacobino, Physical Review A 69, 023809 (2004).
- ²⁵ Y. Pomeau and S. Rica, Comptes Rendus Acad. Sci.(Paris), Série II 317, 1287 (1993).
- ²⁶ L. A. Lugiato and R. Lefever, Physical Review Letters 58, 2209 (1987).
- ²⁷ P. Parra-Rivas, E. Knobloch, D. Gomila, and L. Gelens, Physical Review A 93, 063839 (2016).
- ²⁸ A. Amo, J. Lefrère, S. Pigeon, C. Adrados, C. Ciuti, I. Carusotto, R. Houdré, E. Giacobino, and A. Bramati, Nature Physics 5, 805 (2009).
- ²⁹ M. Van Regemortel and M. Wouters, Physical Review B 89, 085303 (2014).
- ³⁰ A. Vashisht, M. Richard, and A. Minguzzi, SciPost Phys 12, 008 (2020).
- ³¹ F. Claude, M. J. Jacquet, R. Usciati, I. Carusotto, E. Giacobino, A. Bramati, and Q. Glorieux, Physical Review

- Letters 129, 103601 (2022).
- ³² P. Ashwin, S. Wieczorek, R. Vitolo, and P. Cox, Philosophical Transactions of the Royal Society A: Mathematical, Physical and Engineering Sciences 370, 1166 (2012).
- ³³ A. Vanselow, S. Wieczorek, and U. Feudel, Journal of theoretical biology 479, 64 (2019).
- ³⁴ D. Ballarini *et al.*, Nature communications **4**, 1 (2013).
- The results of numerical simulations of the GGPE (Eq. (3)) were obtained by using the semi-implicit Crank-Nicholson code described above, in all figures except Fig. 2a,b. Fig. 2a,b were produced by using a Runge-Kutta code with periodic boundary conditions in a box of size L=38.6823 with a spatial step $\Delta y=0.0377$ and a time step $\Delta t=1.8665\ 10^{-05}$. The high density state was created by a localized zone of strong forcing upstream of the obstacle as in ref.^{7,12} and sketched in Fig. S1. Exploratory and additional simulations were also performed with this other code.
- In Fig. 3, the values of u_m are provided with high precision. They correspond to values obtained within our particular numerical discretization scheme with the chosen spatial step $\Delta y = 0.05$. The obtained high precision critical values u_m^* , of course, approximate the actual ones for the continuous GGPE much less precisely, only to a few percent. We provide the value with high precision since they are required to test Eq. (8). Using these high precision values is meaningful since Eq. (8) holds as well for the discretized equation. In addition, the value of q_+ is only different by a few percent between the discretized GGPE and the continuous one, so we have used the continuous value to check Eq. (8) in Fig. 3f.

(a)



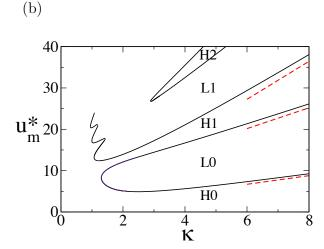


FIG. 6: Reduced asymptotic description. (a) Solutions of Eq. (13),(14) for $\kappa = 2.75$. In the obstacle wake, the flow tends towards the HD-state for $u_m = 4.9$ (dashed orange) and toward the LD-state for $u_m = 5.0$ (dashed-dotted blue). The critical flow corresponds to $u_m^* \simeq 4.93$ (solid red) and tends to the ID-state. (b) Diagram of the transition lines in the (κ, u_m) plane (solid black). The asymptotes for large κ (Eq. (16), (C8), (C14)) of the three lowest transition lines are shown (dashed red). In the different parameter regions, it is indicated whether the flow in the wake of the obstacle tends toward the high (H) or the low (L) density states with the numbers corresponding to the additional 2π dephasing (Eq. (16)) of the large κ solutions in their downstream wake, as compared to the H0 and L0 ones. At finite κ , the boundary between different regions of the same type with different numbers (e.g. H0 and H1) is a line of solutions (not shown) with vanishing density at a point allowing the required phase jump. The zigzagging transition line at $\kappa \simeq 1$ has only been computed up to $u_m^* = 24$. The other parameters are $f = 3.2, \delta_0 = 6.2.$

(a)

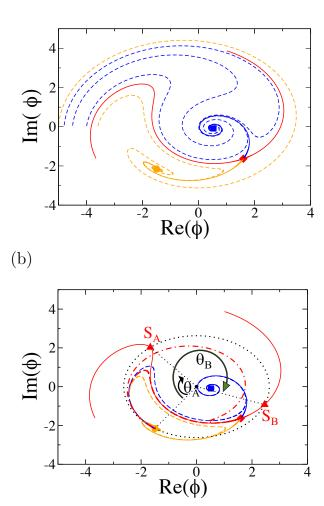


FIG. 7: Phase plane analysis of the reduced asymptotic problem. (a) Phase plane of the homogeneous problem, (Eq. (13), (14)) without the localized potential (i.e. $\delta_V(y) = \delta_0$) showing the three fixed points, HD (orange solid disk), ID (red solid diamond), LD (blue solid square) together with the two entering separatrices (red solid lines) of the ID fixed point and the outgoing ones, ending on the HD point (orange solid line) or the LD point (blue solid line). Several trajectories are also shown ending either on the HD point (dashed orange line) of the LD-state (dashed blue line). (b) Same diagram as (a) but showing two critical trajectories of the reduced problem (Eq. (13), (14)) for $\kappa = 6.0$ with the localized Gaussian potential of amplitude $u_{m,1}^* \simeq 7.328$ (dashed red line) and $u_{m,2}^* \simeq 21.34$ (dashed-dotted red line), corresponding to the first two transitions when u_m is increased from 0. The critical trajectories start in the HD fixed point and they end on the ID fixed point. Two other trajectories are shown which end either at the HD point, with $u_m = 6.5 < u_{m,1}^*$ (dashed orange line), or at the LD point, with $u_m = 8.0 > u_{m,1}^*$ (dashed blue line). It is also shown a circle of radius equal to the modulus of the HD point (dotted black line) centered at the origin (solid black circle) as well as its two intersection points S_1 and S_2 (red triangles) with the entering separatrices of the ID point. The phase difference θ_1 and θ_2 between these intersection points and the HD point are indicated. They provide the asymptotic slopes of the different transition branches (see Eq. (16) and the main text). The other parameters are $f = 3.2, \delta_0 = 6.2.$

Supplementary figure

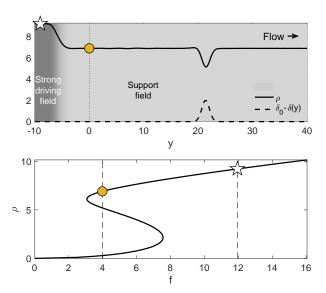


FIG. S1: Schematic description of the experimental setting. The top figure provides a sketch of the experiments (see e.g. ref.[7] and [15] of the main text) that correspond to our theoretical description. The bottom figure shows where the fluid densities in the different regions are located in a bistability diagram (fluid density ρ vs. amplitude of forcing f) similar to Fig. 1a in the main text. On the far upstream side of the obstacle (y < 0 region) a strong resonant driving field (dark grey shade) creates a high density of polaritons (white star in the top and bottom figure). Closer to the obstacle (y > 0 region), the presence of a a weaker "support field" makes the polariton density decrease and stay on the HDstate of a bistability window (solid orange circle) due to the presence of a weaker support field (light grey shade). In this second region, the fluid encounters a repulsive obstacle. In the simulations reported in the main text, only the fluid behavior in the light shaded region is simulated (light shaded region for y > 0 starting at the dotted line). The upstream region with a strong drive is not present, it is simply taken into account by our upstream boundary condition with the fluid on the HD-state (orange circle) of the bistable region.